ADVANCED MATERIALS
www.advmat.de

Acoustophoretic Liquefaction for 3D Printing Ultrahigh-Viscosity Nanoparticle Suspensions

Zheng Liu, Wenyang Pan, Kaiyang Wang, Yoav Matia, Artemis Xu, Jose A. Barreiros, Cameron Darkes-Burkey, Emmanuel P. Giannelis, Yiğit Mengüç, Robert F. Shepherd, and Thomas J. Wallin**

An acoustic liquefaction approach to enhance the flow of yield stress fluids during Digital Light Processing (DLP)-based 3D printing is reported. This enhanced flow enables processing of ultrahigh-viscosity resins (μ_{app} > 3700 Pa s at shear rates $\dot{\gamma}$ = 0.01 s^{-1}) based on silica particles in a silicone photopolymer. Numerical simulations of the acousto–mechanical coupling in the DLP resin feed system at different agitation frequencies predict local resin flow velocities exceeding 100 mm s^{-1} at acoustic transduction frequencies of 110 s^{-1}. Under these conditions, highly loaded particle suspensions (weight fractions, ϕ = 0.23) can be printed successfully in complex geometries. Such mechanically reinforced composites possess a tensile toughness 2000% greater than the neat photopolymer. Beyond an increase in processible viscosities, acoustophoretic liquefaction DLP (AL-DLP) creates a transient reduction in apparent viscosity that promotes resin recirculation and decreases viscous adhesion. As a result, acoustophoretic liquefaction Digital Light Processing (AL-DLP) improves the printed feature resolution by more than 25%, increases printable object sizes by over 50 times, and can build parts >3 × faster when compared to conventional methodologies.

1. Introduction

Additive manufacturing (AM), which encompasses 3D printing, enables the fabrication of complex 3D geometries with precisely prescribed microarchitectures.[1] There are several 3D printing technologies: fused deposition modeling (FDM), ink jetting, selective laser sintering (SLS), direct ink writing (DIW), and vat polymerization, each with a set of trade-offs in terms of cost, compatible materials, available geometries, feature resolution, and print speed.[2,3] For thermosetting polymers, vat polymerization techniques, like Digital Light Processing (DLP) shown in **Figure 1**a, are particularly attractive for the direct fabrication of intricate structures (i.e., overhanging features) while preserving micrometer-scale resolution and rapid deposition rates (>10^6 mm^3 h^{-1}).[4–6]

Despite these potential advantages, the processing steps of conventional DLP restrict compatible materials to low-viscosity photopolymers, which ultimately limits the properties available in the final printed object.[7] During exposure, the photochemical reactions within the liquid resin form chemical bonds between precursors until a percolated network or "gel" forms. The photoirradiation then ceases, and the part is translated one layer in the build direction. Flow within the vat then brings fresh resin into the build area and the process repeats for the next layer. While wiper blades, shearing translations, casting fresh resin, or other modifications can help with fluid flow, in general, many DLP resins possess a low apparent viscosity (μ_{app} < 5 Pa s) for rapid, even replenishment of the next build layer.[8–10] While recoating pastes is trivial even at apparent viscosities as high as 100 kPa s, such methods often fail to fully remove the partially cured, more viscous resin from the walls of the printed object.[11] During the repeated exposures for subsequent layers, this entrained material slowly continues to react, eventually solidifies, and reduces resolution, a problem we refer to as "overcuring". Beyond this loss of resolution, highly viscous materials also create large adhesive forces between the build window and printed object in bottom-up DLP (i.e., methods that draw the build stage up out of the resin during printing). Such adhesive stresses, particularly for large cross-sectional areas, can exceed the strength of

Z. Liu, Y. Matia, A. Xu, R. F. Shepherd
Sibley School of Mechanical and Aerospace Engineering
Cornell University
Ithaca, NY 14853, USA
E-mail: rfs247@cornell.edu

W. Pan, Y. Mengüç, T. J. Wallin
Facebook Reality Labs Research
Redmond, WA 98052, USA
E-mail: thomaswallin@fb.com

K. Wang, C. Darkes-Burkey, E. P. Giannelis, R. F. Shepherd
Department of Materials Science and Engineering
Cornell University
Ithaca, NY 14853, USA

J. A. Barreiros
Department of Systems Science and Engineering
Cornell University
Ithaca, NY 14853, USA

Y. Mengüç
Collaborative Robotics and Intelligent Systems (CoRIS) Institute
Oregon State University
Corvallis, OR 97331, USA

The ORCID identification number(s) for the author(s) of this article can be found under https://doi.org/10.1002/adma.202106183.

DOI: 10.1002/adma.202106183

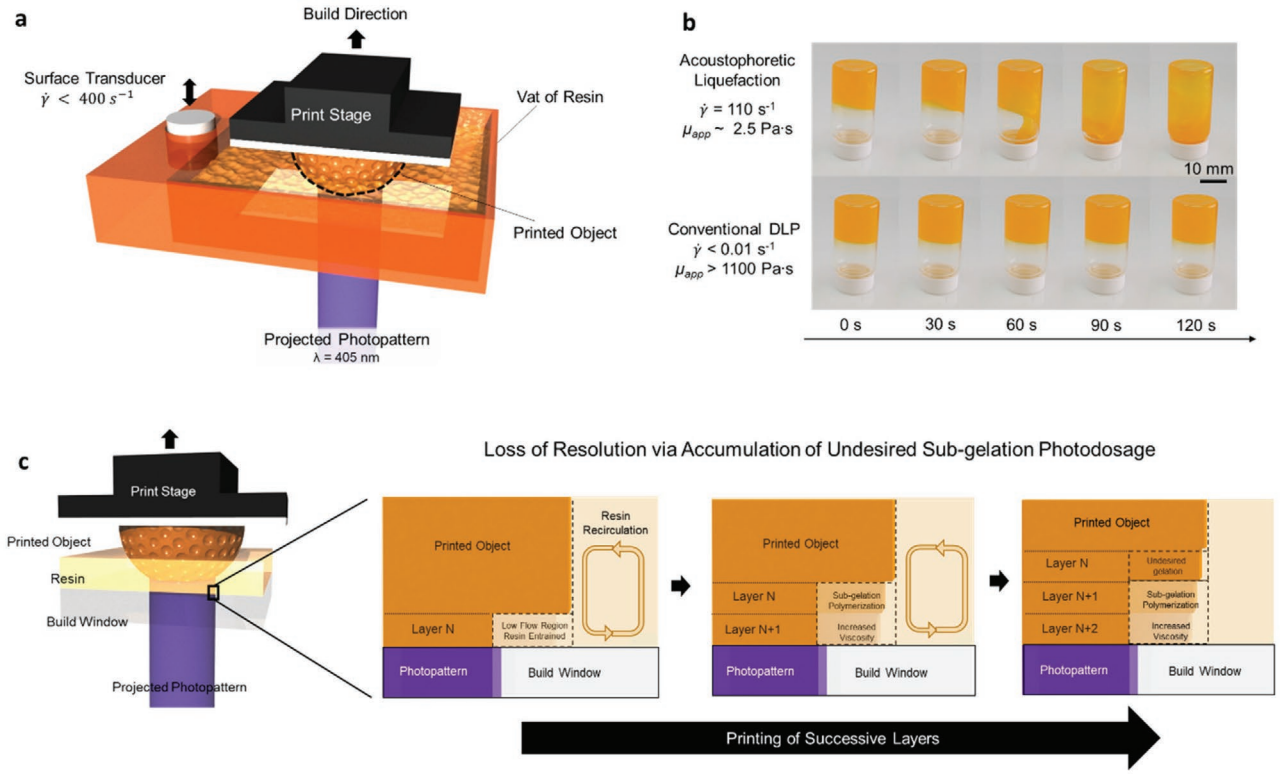

Figure 1. AL-DLP of highly viscous composite resins. a) Schematic of AL-DLP 3D printing hardware. b) Demonstration of acoustophoretic liquefaction using a highly viscoelastic suspension ($\phi = 0.15$) that flows under high-shear-rate conditions but remains static under low-shear-rate conditions (ambient). c) Schematic of "overcuring" in conventional DLP printing of high-viscosity resins where sub-gelation photoexposures result in undesired solidification and loss of resolution over successive layers.

the material and cause failure. While recent advances focused on developing suitable resin chemistries that are compatible with conventional DLP printing,[12–15] many engineering materials, particularly functional composites, remain unprocessable especially in arbitrary geometries due to the implications of viscous precursors.

Polymer–particle composites are a powerful class of materials that allow combinations of functional properties not found in the base components. Among other possibilities, introducing solid nanoparticles into elastomeric matrices can create soft, stretchable materials with enhanced tensile toughness,[16] low electrical resistivity,[17] net magnetization,[18] or high thermal conductivity.[19] These functional properties are dependent on the particle size, surface coating, orientation, and loading fraction. For example, electrical conductivity increases substantially at the volume fraction where conductive fillers first begin to form percolated networks. Unfortunately, from a DLP perspective, the inclusion of particles into prepolymer resins often has a deleterious impact on the rheological properties. Viscosity increases with the volume fraction of fillers as the particle–polymer interactions can create a resistance to flow; this effect is most pronounced around the percolation threshold. While previous work showcases DLP of magnetic, ionic, dielectric, thermal, and piezoelectric composites,[20–25] these works either printed simplistic planar structures or small 3D objects with low volume fractions of fillers ($\phi_{vol} \approx 0.10$), likely due to viscosity related challenges of resin recoating and separation from the build window. Recently, custom heat assisted DLP hardware permitted rheological manipulation of the resin viscosity during processing.[26] By increasing the temperature to 60 °C, researchers printed silica–silicone composite resins with μ_{app} as high as 200 Pa s to improve mechanical properties.[16] However, even at elevated temperatures, the low fluidity of the resin limits printed resolution. The nanoparticle loading also induces light scattering,[27] which results in optical exposure beyond the desired photopattern. This excessive photoexposure can further aggravate issues associated with incomplete resin recirculation, sub-gelation polymerization, and eventually overcuring (Figure 1c). Such undesired solidification adds unwanted fillets at the edges or completely fills negative features (i.e., holes, gaps, overhangs).[28] Ultimately, the rheological and optical phenomena associated with nanoparticles make high-resolution DLP of highly loaded composites still challenging.

Inspired by acoustophoretic droplet-based printing,[29] we developed acoustophoretic liquefaction DLP (AL-DLP) by integrating a surface transducer with the base of the resin vat during printing (Figure 1a). The transducer permits in situ rheological control of non-Newtonian fluids, particularly useful for shear-thinning polymer–particle suspensions like our model silica (i.e., glass microparticles) filled silicone system. As shown in Figure 1b, such materials possess a high viscosity at low shear rates but exhibit a marked drop in viscosity and flow under sufficient shear. To prevent the vibrations from interfering with the photochemical reaction, we program the surface

transducer to operate only in the absence of photoirradiation (i.e., when the build-head raises the part up one-layer height). COMSOL Multiphysics simulations suggest that such a transducer optimized for driving frequency creates local resin velocities up to 110 mm s^{-1}. This agitation promotes resin flow during the interval between optical exposures to simultaneously promote resin recirculation and minimize adhesive forces, which enables processing of highly loaded silica–silicone suspensions with $\mu_{app} > 3700$ Pa s in low-shear-rate conditions ($\dot{\gamma} = 0.01$ s^{-1}). While light scattering can diminish the resolution of a single photoexposure, the combined benefits of the enhancement in resin recirculation, increase in tensile strength, and reduction in viscosity results in an improved resolution for both negative and positive printed features as confirmed by laser scanning confocal microscopy. Further, our rheological manipulation can reduce the viscous adhesion permitting the simple delamination from the build window of large objects with direct vertical translations of the build head. Based on these results, AL-DLP offers rich opportunities for rapid, large-area, high-resolution printing of functional composites based on highly loaded polymer–particle suspensions.

2. Results and Discussion

2.1. Mechanical Properties of the Nanofiller Toughened Thiol–Ene Siloxanes

Silica particles provide mechanical reinforcement in many commercial silicone rubbers.[30] We start by evaluating the mechanical properties of varying filler loadings up to mass fractions $\phi = 0.15$ by conducting uniaxial tensile tests on molded and printed samples. As expected, the results generally show a significant improvement in ultimate elongation, $\varepsilon_{ult} = dL/L_0$ which increases from $\varepsilon_{ult(\phi=0)} \approx 0.7$ to $\varepsilon_{ult(\phi=0.15)} \approx 1.3$ (**Figure 2**a). Additionally, we observed a corresponding tenfold increase in the ultimate tensile strength, σ_{ult}, from ≈50 kPa ($\phi = 0$) to ≈560 kPa ($\phi = 0.15$). Combined, these two trends result in a dramatic increase in tensile toughness, Γ. For printed samples, the $\phi = 0.15$ material possesses a tensile toughness more than 2000% greater ($\Gamma_{(\phi=0.15)} = 375$ kPa) than the neat silicone ($\Gamma_{(\phi=0)} = 18$ kPa). We report full mechanical data in Table S1, Supporting Information.

In conventional composites, the material properties are highly dependent on the particle dispersion in the polymer matrix. For silica–silicone systems, the agglomerated structure of the silica aggregates provides a tortuous path that creates entanglements with the polymer chains.[30] As sonication is known to disrupt microstructure and alter dispersion, we compared the tensile behavior of parts printed with and without acoustophoretic liquefaction ($f = 110$ s^{-1}). As shown in Figure 2a, acoustic agitation does not change the mechanical properties of the printed parts significantly when compared to conventional DLP processing, which suggests that the particle microstructure is similar. For $\phi = 0.15$, printed parts with acoustophoretic liquefaction exhibit a σ_{ult} of 580 ± 70 kPa, while the parts by conventional DLP possess a σ_{ult} of 560 ± 50 kPa. We note that the molded $\phi = 0.15$ samples possess slightly worse ultimate properties than the equivalent material printed via conventional and acoustophouretic liquefaction DLP. Defect size and density dictate failure performance and molding the high-viscosity resins often incorporated microbubbles that were difficult to remove despite our best attempts (see the Experimental Section below). We did not observe such microvoids during printing, likely due to the iterative build motions and small layer heights during printing.

2.2. Rheological Model for DLP Printing Ultrahigh-Viscosity Suspensions

Despite improving the mechanical properties of the printed silicone, increasing ϕ results in a dramatic, and for our purpose, deleterious change of rheological behavior of the DLP resin. For example, under low shear rates ($\dot{\gamma} = 0.01$ s^{-1}), the apparent viscosity increases by almost four orders of magnitude from the neat polymer ($\mu_{app(\phi=0)} \approx 0.2$ Pa s) to the composite ($\mu_{app(\phi=0.15)} \approx$ 1100 Pa s). In fact, the viscosities of silica–silicone composite resins where $\phi > 0.05$ are all much higher than the conventional DLP upper bound ($\mu_{app} = 5$ Pa s[8,9]) and would be unprintable without acoustic agitation (e.g., $\dot{\gamma} >> 0.1$ s^{-1}). Fortunately, as shown in Figure 2b, these materials exhibit shear-thinning

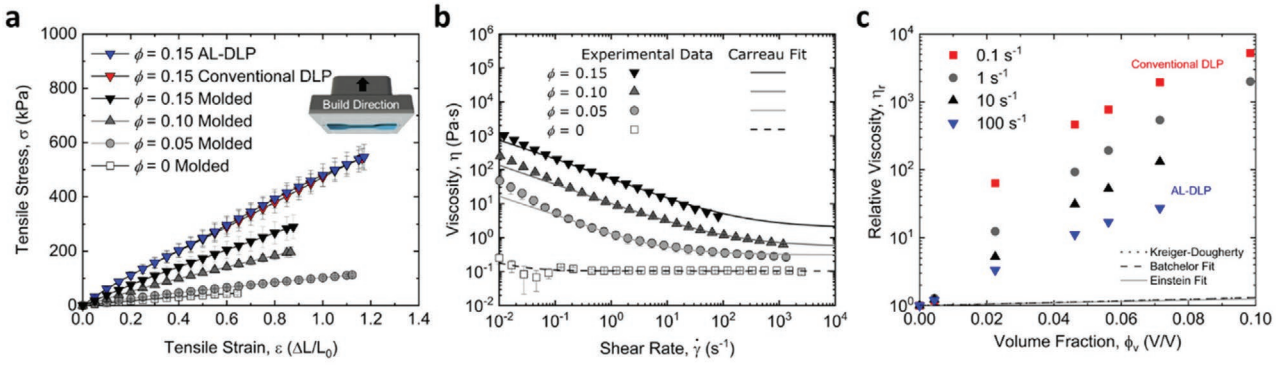

Figure 2. Mechanical and rheological properties of composite resins. a) Average uniaxial tensile tests of the molded silicone at volume fractions, ϕ from 0 to 0.15 ($N \geq 3$), and printed silicones at $\phi = 0.15$ under conventional DLP and with acoustophoretic liquefaction ($N = 3$). b) Average shear dependent viscosity of the different ϕ silica–silicone suspensions ($N = 3$), and $\phi = 0.15$ Carreau model fitted result. c) Relative viscosity of the composite resins relative to the neat resin as a function of volume fraction at different shear rates.

behavior typical of colloidal gels.[31,32] During conventional DLP printing, the vertical movement of the build head in between photoexposures creates an effective shear rate of ≈0.1 s^{-1} as estimated by dividing the vertical velocity by total displacement.[9] Under these conditions, the neat resin ($\phi = 0$) flows easily with $\mu_{app} \approx 0.1$ Pa s. However, for $\phi = 0.15$ at $\dot{\gamma} = 01$ s^{-1}, the resin behaves like a paste with $\mu_{app} \approx 210$ Pa s. Based on the fluid properties of our resins, we use the empirical Carreau model to fit the non-Newtonian behavior.

$$\mu = \mu_{inf} + (\mu_0 - \mu_{inf})\left[1 + (\lambda\dot{\gamma})^2\right]^{\frac{n-1}{2}} \quad (1)$$

where μ_{inf} is the viscosity at an infinite shear rate, μ_0 is the viscosity at zero shear rate, λ is the relaxation time, n is the power index, and μ is the viscosity as a function of the shear rate, $\dot{\gamma}$.[33] For $\phi = 0.15$, $\mu_{inf} = 1.97$ Pa s, $\mu_0 = 1030$ Pa s, $\lambda = 138.10$ s, $n = 0.39$ (see Table S2, Supporting Information, for the model parameters of the other resins). While we acknowledge that the fitted results in Figure 2b diverge from the measured data at low shear rates ($\dot{\gamma} < 0.1$ s^{-1}), the Carreau model generally agrees with experimental values for the higher shear rates relevant to AL-DLP ($\dot{\gamma} >> 0.1$ s^{-1}), particularly when capturing the asymptotic limit to shear-thinning. We find the high-shear-rate viscosities of highly loaded suspensions (i.e., $\phi > 0.15$) unfeasible to directly obtain via rheology due to flow instability and fluid fracture (see Figure S1, Supporting Information). For this reason, we focus our analyses on the $\phi = 0.15$ resin though this does not represent a theoretical limit of the printing methodology—as shown in Figure S3, Supporting Information, we were able to successfully print $\phi = 0.23$ materials which exhibited an apparent viscosity $\mu_{app\ (\phi = 0.23)} > 3700$ Pa s under low shear rates ($\dot{\gamma} = 0.01$ s^{-1}).

We chose our filler particle (i.e., fumed silica) due to its exceptional ability to thicken resins beyond the regime of processible viscosities. As shown in Figure 2c, we see a rapid increase in relative viscosity ($\eta_r = \mu/\mu_{\phi=0}$) at very modest volume fractions of filler ($\phi_v < 0.1$) at experimental shear rates. Like other composite resins based on silica, our measured relative viscosities greatly exceed the expected values of common rheological models by Einstein, Batchelor, and Kreiger–Dougherty[11,16,34] (see Table S3, Supporting Information for details). We attribute these orders of magnitude increase in relative viscosity at low loading to the unique properties of silica. Compared to many ceramic fillers, fumed silica possesses a low density (≈2.2 g cm^{-3}) and flocculates to form complex secondary (aggregates) and tertiary (agglomerate) structures.[30] When the initial polymer–particle dispersion is good, the formation of these tortuous structures entraps and immobilizes large portions of the polymer phase to effectively increase the volume fraction of filler.[35] Thus, our system is particularly challenging to DLP print as it forms ultrahigh-viscosity suspensions at much lower loadings than previously reported composites.[20–25]

2.3. Optical Properties of Silica–Silicone Suspensions

In addition to mechanical reinforcement, nanoparticles often alter the optical properties of the base material, which consequently impact photopolymerization during printing. Limiting the photoexposure to relevant voxels (i.e., volumetric pixels) is critical to achieving high resolution in light-based printing techniques. It is useful to consider separately the resolution of light parallel to the print direction (z) and that of the plane containing the photopattern (x–y). For the former, the attenuation of light within the resin governs the cure depth or how far from the build window interface, the irradiative energy dosage is sufficient for gelation, $H_{e,gel}$. **Figure 3**a shows the absorption, or attenuation of light, as a function of nanoparticles loading in the resin. While the neat polymer is highly transmissive, at $\phi > 0.10$, the optical density, OD, saturates and exceeds the ideal measurement range of the spectrometer. As an alternative, we directly quantify the cure depth by subjecting a vat of resin to a single exposure of increasing photoirradiation dosage, H_e, and measuring the height of the resulting polymerized object. Assuming that light attenuation is described by Beer's Law and the material only solidifies where the applied photodosage exceeds that required for gelation ($H_e > H_{e,gel}$), we can derive a relationship for cure depth, C_d, which describes the z-resolution:[36,37]

$$C_d = D_p \ln\left(\frac{H_e}{H_{e,gel}}\right) = D_p \ln(H_e) - D_p \ln\left(H_{e,gel}\right) \quad (2)$$

where D_p is a constant that captures penetration depth (often the inverse of the product of molar absorptivity and concentration of absorptive species). As shown in Figure 3b, our experimental data agrees closely with this model, with R^2 values approaching unity. Unsurprisingly, the cure depth decreases with increasing particle loading. With an understanding of these "working curves",[38] it is possible to obtain high-z-resolution printing—for example, we recommend selecting an exposure dose per layer that results in a cure depth slightly (≈5–10%) above the desired layer height to ensure interlayer crosslinking. The silica particles decrease cure depth which offers the potential for finer z-resolution. However, it is still possible to obtain such high resolution from the more transmissive resins (e.g., $\phi = 0$) without altering the rheological or mechanical performance by simply reducing the photodosage per layer (i.e., light intensity and/or exposure time) or by adding small aliquots of chemical dyes to increase absorption.[13,14] To further limit cure depth and improve z-resolution, we add 0.008 wt% of orange-colored Sudan I dye in all our printed resins.

The x–y resolution depends on numerous factors including the nominal resolution of the light source, the diffusion of active species (e.g., free radicals) beyond the photopattern, and the scattering of light. While the first two considerations persist even in conventional DLP processes, for composite resins, Rayleigh scattering can dominate as nanoparticle's characteristic length scales fall below the wavelength of photopolymerization ($\lambda = 405$ nm). As the dispersed nanoparticles range from ≈50 nm < d < 500 nm,[30] we expect to observe scattering in the silica suspensions. After excitation at $\lambda = 405$ nm, the emission spectra shown in Figure 3c depict a positive correlation between the ϕ and scattering intensity.

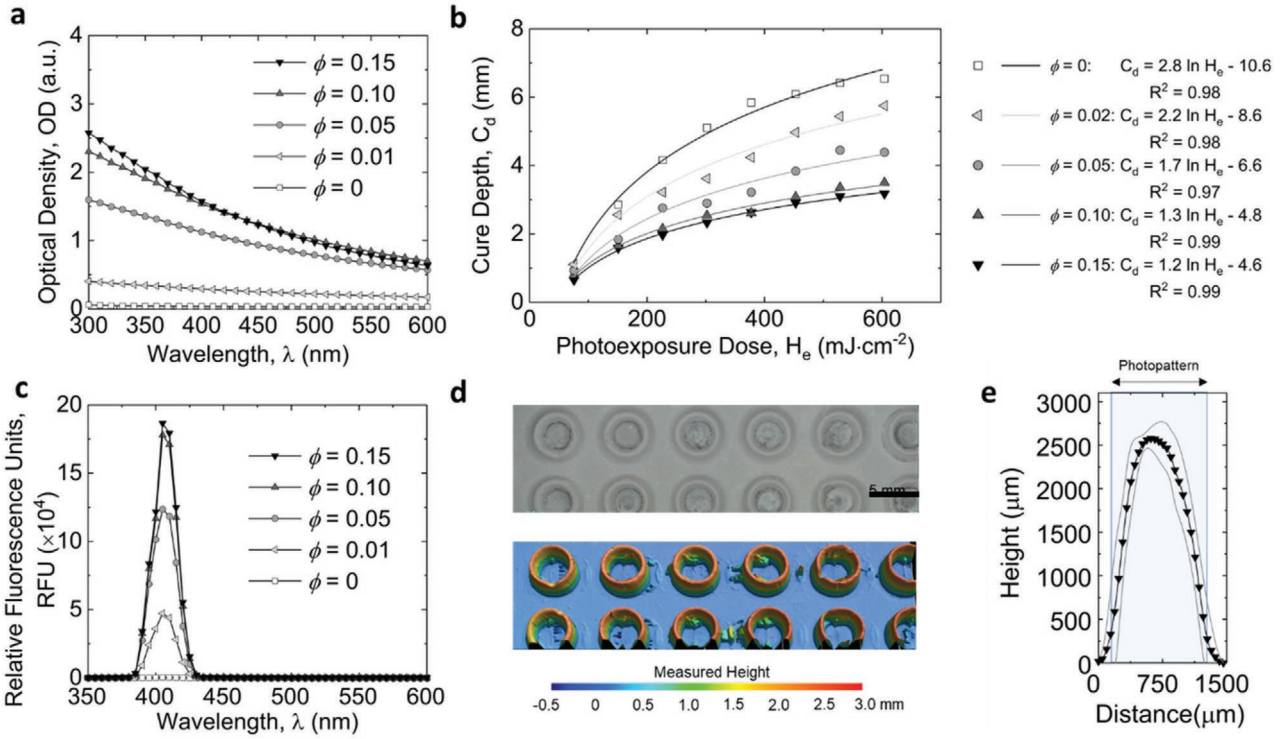

Figure 3. Optical behavior of composite resins. a) Absorption of the silica–silicone suspensions with different ϕ. b) Average cure depth as a function of exposure dose ($N = 7$) with corresponding fits according to Equation (2). c) Scattering of the silica–silicone suspensions with different ϕ, when excited by 405 nm. d) Laser scanning microscopy of an array of printed rings from a scattering resin ($\phi = 0.15$) under a single photoexposure (H_e = 505 mJ cm^{-2}, $\lambda = 405$ nm). e) Average profile ($N = 9$) of printed rings ($\phi = 0.15$) compared to the target profile of the illuminated photopattern. The bounding lines represent standard deviation. See Figure S2, Supporting Information for expanded view.

Nanoparticle scattering is harmful for x–y resolution as it causes light to deviate from its original trajectory in the photopattern. To quantify this effect, we printed an array of ring structures (inner diameter 4 mm, outer diameter 5 mm) with a single photoexposure and used laser confocal microscopy to measure the resulting geometry (see Figure 3d). As shown in Figure 3e, the average profile ($N = 9$) for the composite resin with $\phi = 0.15$ of these rings is 12% (or 0.12 mm) wider than intended at heights 0.3 mm from the build window interface. In these regions, the scattered light exceeds the critical dosage for gelation. At heights of ≈0.6 mm, the measured width matches that of the target photopattern. See Figure S2, Supporting Information for more detail. It is important to note that this result is for a single, prolonged photoexposure whose cumulative dose roughly is ≈10 successive layers during printing (H_e = 45 mJ cm^{-2}, layer height = 30 μm) with no resin recirculation. These conditions are relevant to conventional DLP printing of viscous resins since we expect little fluid flow when the printed object entrains the partially cured resin. As suggested by this experiment, scattered light from subsequent exposures will continue to increase the chemical conversion until the cumulative dosage exceeds $H_{e,gel}$ and material solidifies outside the design. To avoid this significant loss of x–y resolution, we propose acoustophoretic liquefaction in between printing steps to remove this ungelled, partially polymerized material from the build envelope.

2.4. Viscous Adhesion Delamination Criteria and Printable Area

For soft, fine structures, a common failure mode is when the adhesion between the printed object and build window causes the object to fracture while being drawn up out of the vat (see **Figure 4**a). Stefan adhesion describes the force (F) when separating two circular, parallel plates of radius (r) that sandwich a layer of viscous fluid with viscosity (η) and height (h).[39,40] This scenario is similar to separation from the build window in DLP with only vertical translations.

$$F = \frac{3\pi\eta r^4}{2h^3}\frac{dh}{dt} \tag{3}$$

Accordingly, we can approximate the adhesive stress ($\sigma_{adhesion}$) on a printed cylinder during separation by dividing this force by the cross-sectional area. To avoid failure, this adhesive stress must be less than the ultimate strength (σ_{ult}) of the printed part (ignoring deflection and failure of the build-head or build window).

$$\sigma_{ult} > \sigma_{adhesion} = \frac{3\eta r^2}{2h^3}\frac{dh}{dt} \tag{4}$$

While the silica loading increases the ultimate strength by eleven times [$\sigma_{(s,\phi=0)} \approx 50$ kPa to $\sigma_{(s,\phi=0.15)} \approx 560$ kPa], this corresponds to nearly a four order of magnitude increase in the

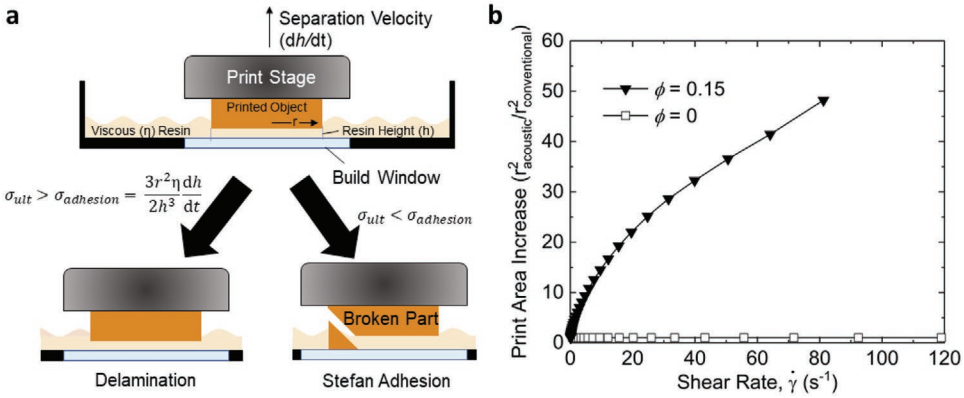

Figure 4. Viscous adhesion and delamination from the build window in AL-DLP. a) The separation process for a printed cylinder of radius, *r*, depending on whether the ultimate strength of the material exceeds the viscous adhesion to the build window. b) The change in printable length scale (print area increase) for the composite material ($\phi = 0.15$) and neat polymer ($\phi = 0$) as a function of applied shear rate based this criterion for separation.

viscosity [$\eta_{(\phi=0)} \approx 0.1$ Pa s to $\eta_{(\phi=0.15)} \approx 210$ Pa s] at low shear rates ($\dot{\gamma} = 0.1$ s^{-1}). As such, the viscosity term dominates, and the adhesive strength exceeds that of the printed material at our length scales (>1 mm). While tuning the processing conditions (e.g., larger layer heights, slower separation speed) can help, this Stefan adhesion often restricts the printable object size for conventional DLP ($\dot{\gamma} \approx 0.1$ s^{-1}) of viscous resins. As shown in Figure 4b, AL-DLP offers a route for large-format printing of highly loaded suspensions. When we fit the previously measured viscosities and ultimate strengths of our materials (see Figure 2), we see a large reduction in Stefan adhesion with applied shear. For our composite material ($\phi = 0.15$), a shear rate of $\dot{\gamma} = 80$ s^{-1} permits delamination from the build window of objects with cross-sectional areas ≈50 times larger than that possible under conventional printing. By comparison, our unfilled pseudoplastic resin ($\phi = 0$) exhibits minimal shear-thinning so we do not see a significant reduction in adhesion and, consequently, no increase in the printable size with acoustophoretic manipulation. Previously reported efforts to DLP print viscous pastes into complex 3D geometries only demonstrate cellular structures or lattices with small cross-sectional areas (≈0.5 cm^2);[11] these designs were likely chosen to minimize adhesion. By driving our acoustic transducer at 300 s^{-1}, we successfully separated printed objects from the build window with cross-sectional areas exceeding 7 cm^2 in even highly loaded systems ($\phi = 0.23$) with apparent viscosities, $\mu_{app} > 3700$ Pa s (see Figures S1 and S3, Supporting Information).

Beyond large format printing, the reduction in viscous adhesion combined with the enhanced resin replenishment allows to only translate the build stage vertically in a method akin to continuous liquid interface production.[5] While all DLP-based methodologies require some vertical motion, printing strategies that accommodate viscous resins further rely on either rotational shear with wiper blades (an additional ≈20 s of horizontal rotation between layers) or hybrid DIW-DLP processes that extrude fresh resin for each layer (an additional ≈10 s per cm^2 of build area for each layer).[10,11,13] Since photoexposure durations are only on the order of a few seconds per layer (e.g., $t_{exposure} = 1.5$ s for $\phi = 0.15$ resin and 30 µm layer), these extraneous steps can represent <90% of the total build time. Though some amount of time between exposures is similarly necessary for acoustic liquefaction, the large resin velocity within $t < 2$s of transduction (as shown in **Figure 5**c, above) suggests the ability to drastically increase print speeds with AL-DLP. Even without further optimization, we can obtain deposition rates ≈10^5 mm^3 h^{-1} at layer heights ≈50 µm due to the combined enhancement in print speeds and printable area that originate from this reduction in viscous adhesion.

2.5. Determining the Location and Driving Frequency of the Surface Transducer

The position and orientation of the surface transducer impact the degree of acoustophoretic liquefaction and resin recirculation. While the placement of the transducer on the build-head promotes agitation immediately below the printed object, we observe that such vibrations can cause permanent misalignment between the build stage and photopattern, which results in poorer resolution. Therefore, we recommend placing the surface transducer in the resin tray outside the build envelope (see Figure 1a). High-speed video of the resin tray shows a net vertical vibration regardless of horizontal or vertical transducer orientation; however, the vertically oriented transducer creates a much higher amplitude (Figure S4, Supporting Information). Also, qualitative examination confirms that the resolution of printed parts with the vertically oriented transducer is superior to that of the horizontally placed transducer (Figure S5, Supporting Information). Thus, we apply the agitation to the base of the resin tray vertically (Figure S6, Supporting Information).

We use a confocal displacement sensor to precisely measure the amplitude of the resin tray under vibration by a vertically oriented surface transducer at different driving frequencies (Figure 5a). We input these amplitudes and frequencies as well as our Carreau rheological model (see above) into COMSOL Multiphysics to obtain a relationship between the frequency of agitation and the velocity profile of resin. By assuming that resin immediately near the printed object is sufficiently entrained such that its velocity in the *y*-direction matches that of the build-head, we can attribute the recirculation of the resin entirely to the fluid velocity in the *x*-direction. Under different frequencies, we calculate the maximum velocity, v_{max}, of the

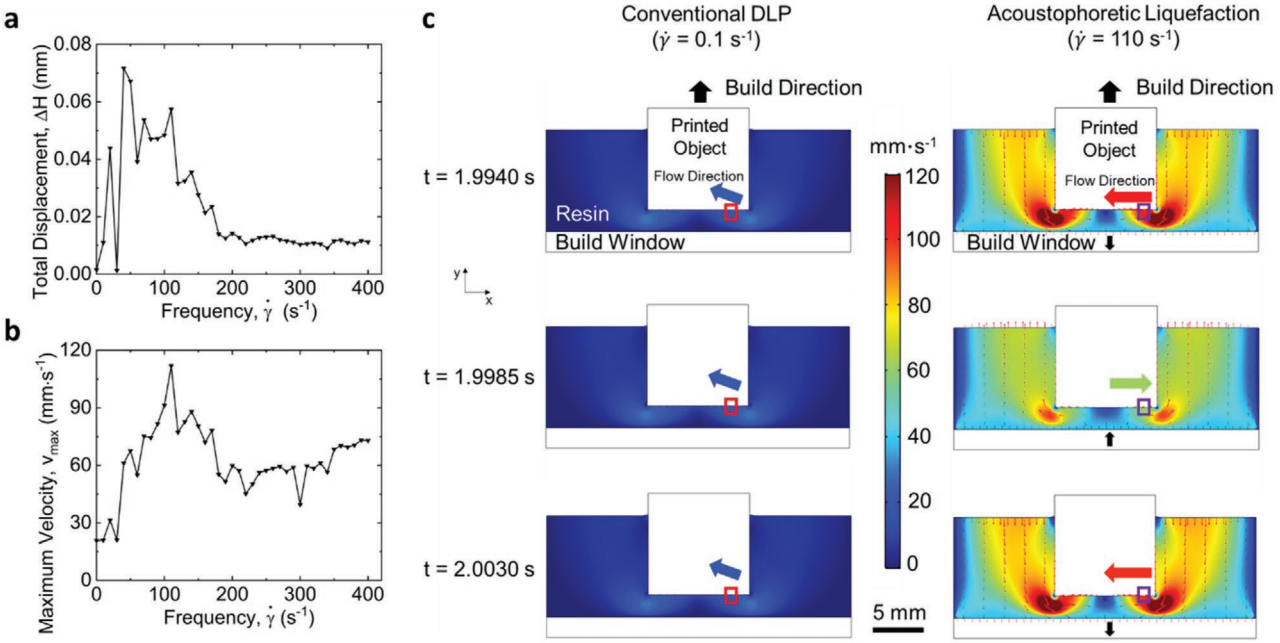

Figure 5. Resin flow under acoustic stimulation. a) Total displacement of the resin tray under different frequencies of vibration, measured by confocal sensor. b) The maximum velocity in the *x*-direction of the resin under different frequencies of vibration by simulation. c) COMSOL simulation result of resin flow (the magnified arrows on the top right represent the direction and magnitude of velocity of the resin near the printed area).

resin near the printed object within the first 2 s of agitation. As shown in Figure 5b, the highest value of v_{max} occurs at a frequency of 110 s^{-1}. Thus, we chose 110 s^{-1} as the optimal f during printing for increasing the flow of $\phi = 0.15$ resin. To confirm that choice, we compare the velocity field of resin during printing with and without acoustophoretic liquefaction. In conventional DLP, ($\dot{\gamma} \approx 0.1$ s^{-1}), Figure 5c clearly shows small resin velocity (<20 mm s^{-1}) throughout the build envelope. This result suggests partially polymerized oligomers will remain entrained near the printed object to increase the risk of undesired gelation with subsequent photoexposures and limit resolution. By comparison, with an acoustic agitation of 110 s^{-1}, local velocities of up to 110 mm s^{-1} promote resin replenishment of the build area.

2.6. Printing Resolution Comparison

Undesired gelation in DLP is particularly troublesome when printing negative features (i.e., holes or gaps) in solid bodies. To evaluate the printed resolution in AL-DLP, we designed and printed a 5 mm × 30 mm × 2mm cuboid with 0.5 mm deep square run through grooves regularly interspersed along with the object. By comparing the quality of these printed structures under a laser-scanning profilometer to the original design file, we can measure the print fidelity with and without acoustophoretic liquefaction. As shown in **Figure 6**a, there is a visible improvement of acoustophoretic liquefaction to conventional DLP. The nominal geometry of the gap being analyzed is 0.5 mm wide and 0.5 mm deep. The gap of the part printed by AL-DLP is closer to the nominal geometry's width with a deeper gap and sharper edges. Considering the vertical cross-sectional area of the printed gap as an indicator of accuracy, the $\phi = 0.15$ AL-DLP part retained ≈80% of the desired gap while the $\phi = 0.15$ part by conventional DLP only printed ≈50% of the target groove. It is important to note that even the neat resin ($\phi = 0$, a simple pseudoplastic fluid, with low viscosity and very low light scattering) does not print with the exact nominal dimensions (printed 70% of the desired gap) highlighting the challenge of resin recirculation in even conventional, unfilled resin systems.

However, we acknowledge that while the depth of the gap improves with acoustic agitation, the measured depth for our printed composite is still only ≈50% that of the target design. These results are consistent with our COMSOL model in Figure 5c; resin flow velocities depend on part geometry, location, and even amount of resin in the vat. At some critical wall height, the effective local shear falls below the threshold for resin recirculation and overcuring occurs. Beyond the well's profile, we also quantified the roughness, or average root mean square height, S_q, on the bottom surface for the $\phi = 0.15$ object. With AL-DLP, this feature is much smoother with mean square root roughness, S_q, ≈18 µm, which is below the 30 µm printed layer height. Comparatively, the S_q of a conventionally DLP printed part is about an order of magnitude worse at 134 µm.

For positive features, as shown in Figure 6b, we successfully printed viscous resin (ϕ = 0.15) into a logo with line widths of 200 µm. Again, without acoustophoretic liquefaction these features are not entirely present, suggesting adhesive failure (i.e., $\sigma_{adhesion} > \sigma_{ult}$) during separation from the build window. Beyond these planar demonstrations of print fidelity, in Figure 6c we demonstrate an enhanced resolution for complex 3D shapes by printing a compliant dimpled semisphere. In a conventional process without acoustophoretic liquefaction, there is an excess of deposited material, particularly around

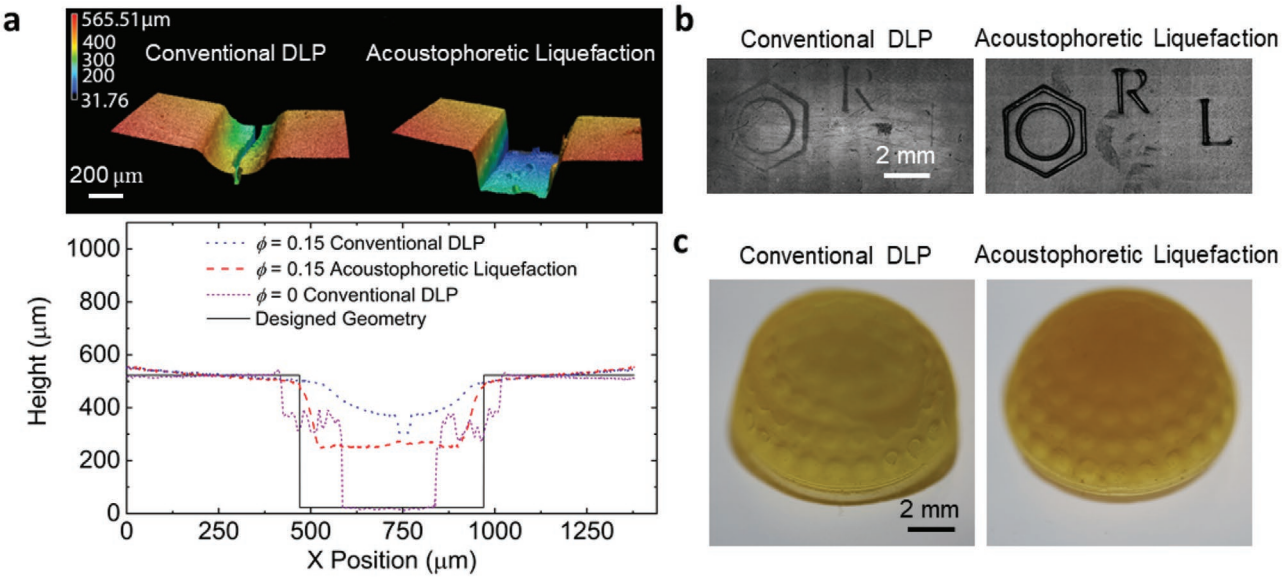

Figure 6. Printed resolution. a) Comparing the surface of printed negative features (500 µm square well) by conventional DLP and with ≈110 s^{-1} acoustophoretic liquefaction from $\phi = 0.15$ resin. b) Printed thin positive features in 2D ($\phi = 0.15$). c) Printed resolution of a semisphere with dimples ($\phi = 0.15$).

the object's base, resulting in an asymmetric print consistent with "overcuring" and poor resin recirculation observed in Figure 3d,e. By comparison, when using AL-DLP, we obtain the more radially symmetric target object with a uniform distribution of dimples. We attribute the improved performance to the enhanced resin flow.

3. Conclusion

We have reported acoustophoretic liquefaction DLP of ultra-high-viscosity nanoparticle suspensions based on surface modified silica in a silicone elastomer resin. As expected, these particle inclusions dramatically increase the tensile toughness (from $\Gamma_{(\phi=0)}$ = 18 kPa to $\Gamma_{(\phi=0.15)}$ = 375 kPa) by simultaneously improving ultimate strength ($\sigma_{ult(\phi=0)}$ from ≈50 kPa to $\sigma_{ult(\phi=0.15)} \approx$ 560 kPa) and elongation ($\varepsilon_{ult(\phi=0)} \approx 0.7$ to $\varepsilon_{ult(\phi=0.15)} \approx 1.3$). However, this particle reinforcement accompanies a change in the prepolymer rheology that hinders conventional vat polymerization printing. We observe a five order of magnitude increase in low-shear ($\dot{\gamma}$ = 0.01 s^{-1}) apparent viscosity (from $\mu_{app(\phi=0)}$ = 0.25 to $\mu_{app(\phi=0.15)}$ = 1100 Pa s) as well as the emergence of significant light scattering at the photopolymerization wavelength (λ = 405 nm). By modifying a DLP printer to incorporate an acoustic transducer, we developed a method for printing such viscous, shear-thinning resins at high resolution (≈100s of µm). An understanding of the shear-thinning behavior and simulation allow us to determine the best frequency for resin replenishment in between photoexposures. For a particle weight fraction of $\phi = 0.15$ in the silicone resin, the model predicts a 110 s^{-1} vertical acoustic agitation providing for a maximum local velocity flow of 110 mm s^{-1} that aids in resin recirculation. Experimentally, such conditions reduce overcuring to enhance printed feature resolution by over 25% when compared to its conventionally printed counterpart. The reduction in apparent viscosity under transduction also offers opportunities for rapid large-format printing—the decrease in viscous adhesion coupled with an increase in ultimate strength permits the separation of printed composite (ϕ = 0.15) objects that are up to 50 × larger by area and the ease of separation with just vertical motions reduces the need for extraneous interlayer operations to reduce build times.

This novel 3D printing methodology is broadly applicable to material chemistries beyond the specific silica–silicone resins used here. Most conventional DLP resins are based on low-molecular-weight monomers and oligomers because viscosity generally increases with polymer molecular weight. Many of these higher-entropy polymer systems (e.g., when the molecular weights exceed the coil to globule transition) are shear-thinning and would benefit from acoustophoretic liquefaction. Further, while this study used spherical silica particles, other anisotropic particles are desirable for many functional composite applications. For example, high-aspect-ratio particles possess a lower percolation threshold, which is required for conductivity, but percolation often accompanies orders of magnitude increase in viscosity.[41] Again, acoustic stimulation aids in the printing of such composite resins that often exhibit a high degree of shear thinning as the high-aspect-ratio particles align parallel to flow.

Beyond simply processing high-viscosity composites, acoustic manipulation offers huge potential for controlling particle orientation, and thereby material properties, for realizing materials with voxelated properties. For example, acoustic flow could create or destroy particle agglomerations for patterning conductivity during DLP. Such functional applications require modeling of the imparted flow fields during acoustophoretic liquefaction. These simulations are computationally costly, and depend on numerous parameters including resin rheology, transducer locations, driving frequencies, transduction amplitudes, and even the geometry and orientation of the printed part. To exert this desired

spatial control over nanoparticle orientation, future hardware developments (i.e., multiple, distributed transducers) must enable selective, localized control over fluid flow. Additionally, as the resin and printed part can viscously dissipate energy to reduce applied shear, large format printing will likely require numerous transducers that provide consistent liquefaction throughout the entire build envelope. Finally, though the process show enhanced resolution, AL-DLP prints of our high-viscosity $\phi = 0.15$ resin still fail to capture negative features finer than ≈200 µm despite our printer possessing a nominal pixel resolution of only 50 µm. Methods that further reduce viscosity, for example, heat-assisted AL-DLP, or promote directed flow (as opposed to oscillatory flow) may aid in removing entrained resin from sophisticated printed architectures at shorter length scales.

4. Experimental Section

Materials: Vinyl terminated poly(dimethylsiloxane) (VS; $M_w \approx$ 6000 Da) and [4–6% (mercaptopropyl)methylsiloxane]-dimethylsiloxane (MS; $M_w \approx$ 7000 Da) (Gelest, Inc., Morrisville, PA, USA) were mixed to prepare the pristine resin (5% VS6000) with a stoichiometric ratio of 1 mercapto (thiol) group per 1 vinyl (-ene) group. A liquid photoinitiator blend (20 wt% diphenyl(2,4,6-trimethylbenzoyl) phosphine oxide in 80 wt% 2-hydroxy-2-methylpropiophenone) (Sigma–Aldrich Co., St. Louis, MO, USA) was added to the resin at the concentration of 1 wt%. Sudan I (Sigma–Aldrich Co., St. Louis, MO, USA), previously dissolved in a toluene stock solution, was also added as the light-absorbing agent at a final Sudan concentration of 0.08 mg mL^{-1} resin to improve the resolution along the *Z*-axis by reducing the penetration depth of the light in the resin.

The PDMS was compounded with functionalized fumed silica R202 (Evonik Industries, Allentown, PA, USA) into the 5% VS6000 siloxane resin at varying mass fractions (from $\phi = 0$ to $\phi = 0.23$), using a Thinky ARM 310 mixer (THINKY, Laguna Hills, CA, USA) at 2000 rpm for three cycles (30 s per cycle).

Rheology Measurements: To measure the viscosity of the silica–silicone suspensions, we performed shear rheological measurements using an MCR 702 rheometer (Anton Paar, Graz, Austria), at a shear rate of $0.01 \leq \dot{\gamma} \leq 1000\ s^{-1}$. Since we could not use concentric cylinder measuring systems or double-gap measuring systems due to the high viscosity, they chose cone-plate measuring systems over parallel-plate measuring systems to achieve the uniform shear conditions in the entire conical gap.[42]

Mechanical Tests: The mechanical properties of the cured elastomers were tested by photocuring dog-bone shaped samples (width = 6.4 mm, depth = 3.0 mm, gage length = 40 mm) using an Omnicure 1500 UV light source (Excelitas Technologies, Waltham, MA, USA) by molding. To ensure consistent photocuring, we subjected both sides of the acrylic mold to >500 mJ cm^{-2} of exposure. During the molded high viscosity ($\phi < 0.1$), samples often possess numerous visible air bubbles in the resin. We minimized these defects by utilizing a pressure pot (dP ≈ 80 PSI) for 20 min after casting but prior to photocuring. We also 3D printed samples with the gauge area parallel to the build plate to investigate the impact of the manufacturing process on mechanical performance. Surprisingly, bubbles in the high-viscosity resins were not as visually apparent during printing (both through conventional DLP and AL-DLP), likely due to the applied shear and recoating. We conducted uniaxial tensile tests using Zwick & Roell Z1010 testing machine (Ulm, Germany) at a strain rate of 1.0 min^{-1}. For the molded samples, we used the nominal, designed geometry when calculating engineering stress and engineering strain. The dimensions of 3D printed samples were measured prior to each test with digital calipers.

Spectrophotometry: A UV–vis plate reader (Molecular Devices, San Jose, CA, USA) was used to measure the absorption and scattering of the silica-silicone suspensions from 300 to 600 nm for absorption.

Cure Depth and Scattering Measurements: With the build head removed, the build envelope was filled with resin ≈5 mm deep. We then exposed this resin to an array of circles (d = 10 mm) for single exposures of increasing time. After rinsing in isopropyl alcohol and gently removing ungelled material with a cotton swab, the height of the resulting cylinders was measured with calipers, averaging over eight measurements. For scattering measurements, arrays of rings (outer diameter = 5 mm, inner diameter = 4 mm) were simply projected during a single exposure step. The intensity of the photopattern was measured at the build window as 30.1 mW cm^{-2} using a radiometer (Model 222, 405 nm probe, G & R Labs).

Acoustophoretic Liquefaction DLP: A commercial Ember DLP printer (Autodesk, San Rafael, CA, USA), with a blue LED projector (λ = 405 nm, E_e = 22.5 mW cm^{-2}) was modified for our purposes. Originally, the printer programming rotated the vat between layers to delaminate the printed object from the window. However, implementing the rotation may damage the ongoing prints or even push off the build-head due to the ultrahigh viscosity in our study. Inspired by continuous liquid interface production (CLIP),[5] the printer's code was altered to only perform vertical movements to separate the printed part from the build window. This modification reduced the possibility of damaging the printed part and significantly reduced the printing time. Using this strategy, it was found that the adhesion forces between the build window and the printed part played a more important role in successful printing.[4] Therefore, an Epilog Zing 24 laser cutter (Epilog Laser, Golden, CO, USA) was used to cut 2 mm TPX polymethylpentene (PMP) (Goodfellow, Coraopolis, PA, USA) into the shape of our build window and adhere the window to the resin tray (See Figure S7, Supporting Information) using Sil-Poxy (Smooth-On, Inc, Macungie, PA, USA). For our printing experiments, a *z*-layer height of 30 µm was selected. In between processing steps, the ongoing print was translated 5 mm upwards with the build-head, the resin replenished the build area, and then the build-head returned 4.97 mm (establishing the preset layer thickness of 0.03 mm) before the next optical exposure. The Print Studio software (Autodesk, version 1.6.5) sliced the 3D model into 0.03 mm layers which were then each projected sequentially to print the file.

To enable acoustic liquefaction, we installed an LB07 surface transducer (Digi-Key, Thief River Falls, MN, USA) to the base of the resin tray (see Figure S6a, Supporting Information). An Arduino Uno (Digi-Key, Thief River Falls, MN, USA) was installed and the signal of the surface transducer synchronized with that of the build head's stepper motor. This ensured that the acoustic transducer only operated when the build-head was moving and not while the photopattern was projected. A Pololu 3081 encoder (Pololu, Las Vegas, NV, USA) placed on the stepper motor recorded this movement. When the build-head was moving, the Arduino Uno provided a pulse width modulation signal to an Alpine MRV-M500 amplifier (Alpine electronics, Torrance, CA, USA). To avoid the movement of the resin tray from hitting the ongoing prints, the signal was sent 1 s after the build-head started moving up and continued until 1 s before the build-head arrived at the target height. Thus, the ongoing prints were at least 1 mm away from the build window based on the speed of the build-head (1 mm s^{-1}). We powered the amplifier with a power supply (Xizu, Las Vegas, NV, USA) at 12 volts (see Figures S8 and S9, Supporting Information).

Movement Measurements: We used a Phantom Miro 310 high-speed camera (Vision Research, Inc. Wayne, NJ, USA) at 1000 fps and 256 × 128 pixels to record the movement of the resin tray under agitation and determine the amplitude of the resin tray under different frequencies of agitation using ImageJ.

A DT 2451 confocal sensor (Micro-Epsilon, Ortenburg, Germany) with 10 kHz measuring rate and 1 nm resolution was used to obtain more precise amplitudes of the resin tray with the vertically oriented surface transducer. Since the amplifier could not amplify the signal higher than 400 Hz, we analyzed the movement of the resin tray from 10 to 400 Hz in 10 Hz increments.

COMSOL Model: Seeking to quantify the relationship between the frequency of the agitation and the resin circulation, we used COMSOL 5.6 (COMSOL, Inc., Burlington, MA, USA) to simulate the resin flow under print conditions. They examined the short period following the cessation of illumination, when the system replenished the resin volume underneath the printed object as it moved up between layer polymerization.

Following the Multiphysics concept of the software, we used a two-way coupled fluid–structure interaction module in a 2D domain. The fluid domain was a cross-section area 30 mm wide (in the *x*-direction) and 10 mm high (in the *y*-direction). Fluid properties include $\rho = 1115$ kg m^{-3} and dynamic viscosity modeled, where we used the non-Newtonian Carreau model, see above Equation (1), and the rheological fitted result of $\phi = 0.15$ resin. The fluid domain interacted with two solid domains: First, positioned underneath the fluid domain; we set a solid domain 30 mm wide (in the *x*-direction), 2 mm high (in the *y*-direction) representing the build window supporting the fluid domain from below. The second solid is the printed object 10 mm wide and 10 mm high starting 1.98 mm above the build window domain.

Realizing the printing process, the printed object domain was given a prescribed velocity of $(u_h, v_h) = (0,\ 1)$ mm s^{-1}, while the build window oscillated in the *y*-direction governed by being given a prescribed velocity $(u_w, v_w) = (0,\ \pi f \Delta H \cos(2\pi f t))$ mm s^{-1}, in which frequency, f, and corresponding total displacement, ΔH, are measured by confocal displacement sensor (Figure 5a). In doing so, we introduced a shear rate $\dot{\gamma}$ leading to the shear thinning of the resin (the above mentioned acoustic liquefaction), thus increasing the influx of resin driven by pressure and gravity-driven flows. A gravity volume force was set in the fluid domain $g = 9.81$ m s^{-2}, and atmospheric pressure applied to the top surface, that is, the open face of the fluid domain at $y = 12$ mm on both sides of the printed object. In addition, the No-slip condition was set to all fluid domain walls as well as printed object and build window wetted surfaces.

The discretization consisted of linear Lagrange elements in the fluid domain and quadratic Lagrange elements for the solid domain. The mesh consisted of $O(10^3)$ domain elements and $O(10^2)$ boundary elements along wetted walls surfaces, corresponding to a total of $O(10^4)$ DOF solved.

Laser Confocal Microscopy: A Keyence VK-X260 laser-scanning profilometer (Keyence, Itasca, IL, USA) with 10× objective was used to optically profile the printed parts' surfaces. We processed this data via MultiFileAnalyzer (Keyence, version 1.3.1.120).

Supporting Information

Supporting Information is available from the Wiley Online Library or from the author.

Acknowledgements

The authors thank Shuo Li, Hedan Bai, Maura O'Neill, Ronald Heisser, Chengyu Liu, and Yucheng Chen for helpful discussions. The authors thank Di Ni, Benyamin Davaji, and Adarsh Ravi for assistance on confocal sensor tests. The authors would like to acknowledge Viktor Lifton and Evonik for providing both research quantities of silica and technical support. The authors also thank Autodesk for generously gifting 3D printing hardware to contributing laboratories at Cornell. Portions of this study were performed at Cornell Center for Materials Research Shared Facilities and the Cornell Energy Systems Institute. These facilities are supported in part by NSF MRSEC program (Grant No. DMR-1719875).

Conflict of Interest

R.F.S. is a board member of the Organic Robotics Corporation. All other authors declare that they have no conflict of interest.

Data Availability Statement

The data that support the findings of this study are available from the corresponding author upon reasonable request.

Keywords

3D printing, functional materials, polymer composites

Received: August 8, 2021
Revised: September 24, 2021
Published online: January 5, 2022

[1] D. K. Patel, A. H. Sakhaei, M. Layani, B. Zhang, Q. Ge, S. Magdassi, *Adv. Mater.* **2017**, *29*, 1606000.
[2] R. L. Truby, J. A. Lewis, *Nature* **2016**, *540*, 371.
[3] T. J. Wallin, J. Pikul, R. F. Shepherd, *Nat. Rev. Mater.* **2018**, *3*, 84.
[4] D. A. Walker, J. L. Hedrick, C. A. Mirkin, *Science* **2019**, *366*, 360.
[5] R. Janusziewicz, J. P. Rolland, J. R. Tumbleston, N. Ermoshkin, D. Kelly, A. R. Johnson, R. Pinschmidt, D. Shirvanyants, A. Ermoshkin, J. M. DeSimone, K. Chen, E. T. Samulski, *Science* **2015**, *347*, 1349.
[6] B. E. Kelly, I. Bhattacharya, H. Heidari, M. Shusteff, C. M. Spadaccini, H. K. Taylor, *Science* **2019**, *363*, 1075.
[7] Y. Luo, G. L. Fer, D. Dean, M. L. Becker, *Biomacromolecules* **2019**, *20*, 1699.
[8] M. Li, K. G. Neoh, L. Q. Xu, R. Wang, E. T. Kang, T. Lau, D. P. Olszyna, E. Chiong, *Langmuir* **2012**, *28*, 16408.
[9] C. Hinczewski, S. Corbel, T. Chartier, *Rapid Prototyping J.* **1998**, *4*, 104.
[10] D. A. Rau, M. Forgiarini, C. B. Williams, *Addit. Manuf.* **2021**, *42*, 101996.
[11] N. Rodriguez, S. Ruelas, J. Forien, N. Dudukovic, J. Deotte, J. Rodriguez, B. Moran, J. P. Lewicki, E. B. Duoss, J. S. Oakdale, *Polymers* **2021**, *13*, 2239.
[12] M. Podgórski, S. Huang, C. N. Bowman, *ACS Appl. Mater. Interfaces* **2021**, *13*, 12789.
[13] T. J. Wallin, L. E. Simonsen, W. Pan, K. Wang, E. Giannelis, R. F. Shepherd, Y. Mengüç, *Nat. Commun.* **2020**, *11*, 4000.
[14] T. J. Wallin, J. H. Pikul, S. Bodkhe, B. N. Peele, B. C. Mac Murray, D. Therriault, B. W. McEnerney, R. P. Dillon, E. P. Giannelis, R. F. Shepherd, *J. Mater. Chem. B* **2017**, *5*, 6249.
[15] S. Li, H. Bai, Z. Liu, X. Zhang, C. Huang, L. W. Wiesner, M. Silberstein, R. F. Shepherd, *Sci. Adv.* **2021**, *7*, eabg3677.
[16] K. Wang, W. Pan, Z. Liu, T. J. Wallin, G. Van Dover, S. Li, E. P. Giannelis, Y. Menguc, R. F. Shepherd, *Adv. Mater.* **2020**, *32*, 2001646.
[17] K. P. Sau, D. Khastgir, T. K. Chaki, *Angew. Makromol. Chem.* **1998**, *258*, 11.
[18] S. Ijaz, H. Li, M. C. Hoang, C. S. Kim, D. Bang, E. Choi, J. O. Park, *Sens. Actuators, A* **2020**, *301*, 111707.
[19] M. D. Bartlett, N. Kazem, M. J. Powell-Palm, X. Huang, W. Sun, J. A. Malen, C. Majidi, *Proc. Natl. Acad. Sci. USA* **2017**, *114*, 2143.
[20] W. Zhu, J. Li, Y. J. Leong, I. Rozen, X. Qu, R. Dong, Z. Wu, W. Gao, P. H. Chung, J. Wang, S. Chen, *Adv. Mater.* **2015**, *27*, 4411.
[21] K. Kim, W. Zhu, X. Qu, C. Aaronson, W. R. McCall, S. Chen, D. J. Sirbuly, *ACS Nano* **2014**, *8*, 9799.
[22] J. Odent, S. Vanderstappen, A. Toncheva, E. Pichon, T. J. Wallin, K. Wang, R. F. Shepherd, P. Dubois, J. M. Raquez, *J. Mater. Chem.* **2019**, *7*, 15395.
[23] J. J. Martin, B. E. Fiore, R. M. Erb, *Nat. Commun.* **2015**, *6*, 8641.
[24] U. Kalsoom, A. Peristyy, P. N. Nesterenko, B. Paull, *RSC Adv.* **2016**, *6*, 38140.

[25] A. Malas, D. Isakov, K. Couling, G. J. Gibbons, *Materials* **2019**, *12*, 3818.
[26] T. Kuhnt, F. L. C. Morgan, M. B. Baker, L. Moroni, *Addit. Manuf.* **2021**, *46*, 102102.
[27] C. Sun, X. Zhang, *J. Appl. Phys.* **2002**, *92*, 4796.
[28] J. Madrid-Wolff, A. Boniface, D. Loterie, P. Delrot, C. Moser, arXiv: 2105.14952, **2021**.
[29] D. Foresti, K. T. Kroll, R. Amissah, F. Sillani, K. A. Homan, D. Poulikakos, J. A. Lewis, *Sci. Adv.* **2018**, *4*, eaat1659.
[30] Evonik Industries AG, "AEROSIL-Fumed Silica Technical Overview," **2015**, https://www.silica-specialist.com/product/aerosil/downloads/technical-overview-aerosil-fumed-silica-en.pdf.
[31] J. E. Smay, G. M. Gratson, R. F. Shepherd, J. Cesarano, J. A. Lewis, *Adv. Mater.* **2002**, *14*, 1279.
[32] M. T. Roberts, A. Mohraz, K. T. Christensen, J. A. Lewis, *Langmuir* **2007**, *23*, 8726.
[33] M. W. Siebert, P. S. Fodor, in *Proc. COMSOL Conf. 2009 Boston*, COMSOL, Burlington, MA, USA **2009**, p. 27, https://www.comsol.com/paper/download/44844/Fodor.pdf.
[34] C. O. Metin, R. T. Bonnecaze, Q. P. Nguyen, *Appl. Rheol.* **2011**, *21*, 13146.
[35] J. Wen, D. Bryant, *Fumed Silica Controls Rheology of Adhesives and Sealants*, *Adhesives & Sealants Industry*, August **1999**, https://www.adhesivesmag.com/articles/85787-fumed-silica-controls-rheology-of-adhesives-and-sealants.
[36] J. H. Lee, R. K. Prud'homme, I. A. Aksay, *J. Mater. Res.* **2001**, *16*, 3536.
[37] J. Bennett, *Addit. Manuf.* **2017**, *18*, 203.
[38] P. F. Jacobs, *Rapid Prototyping and Manufacturing: Fundamentals of Stereolithography*, Society of Manufacturing Engineers, Southfield, MI, USA **1992**.
[39] Y. Chen, J. Meng, Z. Gu, X. Wan, L. Jiang, S. Wang, *Adv. Funct. Mater.* **2020**, *30*, 1905287.
[40] B. Adzima, *The Ember Printer: An Open Source for Software, Hardware, and Materials Development* **2015**.
[41] J. S. Park, T. Kim, W. S. Kim, *Sci. Rep.* **2017**, *7*, 3246.
[42] T. G. Mezger, *Applied Rheology: With Joe Flow on Rheology Road*, Anton Paar, Graz, Austria **2015**.